Comput Mech (2012) 50:1–18
DOI 10.1007/s00466-011-0665-7

ORIGINAL PAPER

A two-level mesh repartitioning scheme for the displacement-based lower-order finite element methods in volumetric locking-free analyses

C. T. Wu · W. Hu

Received: 9 May 2011 / Accepted: 16 November 2011 / Published online: 14 December 2011

Abstract We present an approach for repartitioning existing lower-order finite element mesh based on quadrilateral or triangular elements for the linear and nonlinear volumetric locking-free analysis. This approach contains two levels of mesh repartitioning. The first-level mesh re-partitioning is an h-adaptive mesh refinement for the generation of a refined mesh needed in the second-level mesh coarsening. The second-level mesh coarsening involves a gradient smoothing scheme performed on each pair of adjacent elements selected based on the first-level refined mesh. With the repartitioned mesh and smoothed gradient, the equivalence between the mixed finite element formulation and the displacement-based finite element formulation is established. The extension to nonlinear finite element formulation is also considered. Several linear and non-linear numerical benchmarks are solved and numerical inf-sup tests are conducted to demonstrate the accuracy and stability of the proposed formulation in the nearly incompressible applications.

Keywords Finite element · Penalty method · Locking-free · Nonlinear · Gradient smoothing

1 Introduction

The volumetric locking in displacement-based lower-order finite element methods has been studied extensively and many special numerical techniques have been proposed to resolve this difficulty. Representative approaches are mixed method [45], reduced/selective integration [21], reduced integration and hourglass control/stabilization method [9,26], equal-order interpolation with stabilization method [2,22], assumed strain method [28,35], discontinuous Galerkin methods [4,19] average nodal pressure element [10] and methods based on gradient or pressure smoothing [20,41] via macro-element technique [36]. The $Q_1 - P_0$ mixed element, continuous piecewise bilinear for displacement and piecewise constant for pressure on quadrilateral element, is probably the simplest element used to overcome the volumetric locking problem. However the stability of this element is strongly mesh-dependent. Namely, the inf-sup condition established in [7,11] holds on some meshes but fails on the others. As a result the solutions may display acceptable displacement but spurious pressure. Several pressure smoothing procedures [21] were developed to perform the necessary filtering as a byproduct. Despite this inconvenience, $Q_1 - P_0$ mixed element remains one of the popular elements used in the finite element method for nearly-incompressible analysis. Hughes's reduced/selective integration has a close link [29] with the mixed formulation where the displacement and implicit pressure interpolant spaces are still subjected to an inf-sup condition for the stability requirement. A mean to circumvent the inf-sup condition in the mixed equal-order finite element formulation is to add a residual of the momentum equation as a stabilization term [22]. Attention also has been paid to the solving of the volumetric locking problem by discontinuous Galerkin (DG) method [19]. DG method can be considered as a class of interior penalty method where jump discontinuities are allowed in the neighboring elements and a consistent interface formulation is derived by refraining from the use of penalty method. DG method is closely related to the classical nonconforming Crouzeix–Raviart (CR) element [15] which is known to be unstable for the traction problem in linear elasticity. Hansbo and Larson [19] introduced the CR element approximation in DG method and obtained a stable version of the CR element in the mixed form of

C. T. Wu (✉) · W. Hu
Livermore Software Technology Corporation, Livermore, CA 94550, USA
e-mail: ctwu@lstc.com

elasticity equations for near-incompressible problem. A general analysis of DG methods for elliptic problems can be found in [4]. Recently a pressure gradient stabilization method was proposed by Areias et al. [2] to stabilize the unstable displacement/pressure pairs without residuals. In reduced integration and stabilization method [26], an assumed strain field [35] is obtained by the Taylor expansion of displacement gradient matrix and the resulting discrete equation can be expressed explicitly by one-point quadrature terms and their stabilization. Since the pioneering work by Bonet et al. [10] various average nodal pressure formulations have been developed (cf. e.g. [1,24]) to overcome incompressible locking. A priori error estimate [25] using primal and dual meshes reveals that original average nodal pressure formulation does not satisfy a uniform inf-sup condition. In order to have a stable formulation, the linear displacement space needs to be enriched with bubble functions as in the mini-element [3]. This analysis leads to a consistent variational framework for the stabilized nodally integrated tetrahedral presented by Puso et al. [33]. A parallel idea of averaging nodal pressure is to average the pressure or deformation gradient fields [20,41] over the macro-element. A carefully chosen displacement space on sub-elements and pressure space on macro-element with a view to satisfying the inf-sup condition leads to the uniform convergence in the nearly incompressible case.

Several non-conventional volumetric locking-free methods also have been developed as alternative to solve the near-incompressible problem. A pseudo-divergence-free interpolation for Element-free Galerkin method [8] was proposed by Vidal et al. [39] to diffuse the divergence-free constraint which can be imposed a priori in a displacement-based Galerkin meshfree formulation. A locking-free Reproducing Kernel Particle formulation [27] was presented by Chen et al. [13] for the nonlinear analysis of rubber-like materials. Subsequently, various meshfree approaches have also been developed to alleviate the volumetric locking [16,17,31] in the framework of B-bar or mixed formulations. Recently, the iso-geometric discretization based on Non-Uniform Rational B-Splines (NURBS) [19] has presented an interesting alternative to solve the incompressible or near-incompressible problems. The high continuity of the NURBS interpolation allows us to solve the incompressible elasticity as an elliptic fourth-order problem in terms of a scalar stream function [5]. A nonlinear F-bar projection method [18] using the higher-order NURBS interpolation was also proposed for solving the nonlinear near-incompressible elasticity problem. More recently, a displacement-based meshfree-enriched finite element method (ME-FEM) was proposed by Wu and Hu [42] to overcome the volumetric locking in linear triangular and tetrahedral elements for near-incompressible elasticity problem. The approximation in ME-FEM element is established by introducing a first-order convex meshfree approximation [32,43,44] into a linear finite element with an enriched meshfree node. An area-weighted strain smoothing technique [42] is developed to acquire the discrete divergence-free approximations in ME-FEM elements for the volumetric locking-free analysis. An equivalent mixed formulation was derived in [42] and numerical inf-sup test [6] was studied. Their results suggest that the pair of spaces of displacement and pressure fields in meshfree-enriched finite element method is inf-sup stable.

The two-level mesh repartitioning scheme presented in this paper is motivated by the idea of element-wise meshfree enrichments and area-weighted strain smoothing technique from the meshfree-enriched finite element method [42] for the volumetric locking-free analysis. The reminder of the paper is outlined as follows: In the next Section, we provide an overview on the fundamental equations and stability requirements of mixed finite element method for nearly incompressible elasticity problems. In Sect. 3, we present the two-level mesh repartitioning scheme for finite element method based on quadrilateral and triangular elements. A constraint count for the new partitioned mesh is studied. In addition, a connection between mixed finite element formulation and displacement-based finite element formulation is established under the new partitioned mesh using the strain smoothing technique. In Sect. 4, a Total Lagrangian formulation using the two-level mesh repartitioning scheme is presented for the nonlinear hyper-elasticity problem. A mixed three-field Hu–Washizu–de Veubeke variational principle [40] is employed to formulate the problem and a displacement-based discrete equation is derived. Several numerical examples are presented in Sect. 5 to demonstrate the accuracy and stability of the proposed method for the linear and nonlinear volumetric locking-free analyses. Final remarks are given in Sect. 6.

2 Review of fundamental equations

Consider a plane-homogeneous isotropic linear elastic body which occupies a bounded polygonal domain Ω in $\mathbb{R}^2$ with boundary $\Gamma = \partial\Omega$ and is under the action of external and internal forces. The strong form of the boundary-value problem for nearly incompressible cases can be stated by the following [21]:

$$\begin{cases} \sigma_{ij,j} + b_i = 0 & \text{in } \Omega \\ u_{i,i} + p/\lambda = 0 & \text{in } \Omega \end{cases} \tag{1}$$

with the boundary conditions

$$u_i = g_i \text{ on } \Gamma_g \tag{2}$$

$$\sigma_{ij} n_j = h_i \text{ on } \Gamma_h \tag{3}$$

where σ_{ij} is the Cauchy stress tensor, b_i is the components of body forces, u_i is the displacement components, p is the

pressure parameter which is viewed as an independent unknown, g_i is the prescribed boundary displacements, n_i is the unit outward normal vector, and traction h_i is distributed over the Neumann boundary Γ_h with $\Gamma = \Gamma_g \cup \Gamma_h$ and $\Gamma_g \cap \Gamma_h = 0$. With the fourth-order elasticity tensor denoted by $\boldsymbol{C}$, the constitutive equation is given by

$$\boldsymbol{\sigma} = \boldsymbol{C}\varepsilon = 2\mu\varepsilon + \lambda\,(tr\varepsilon)\,\boldsymbol{I} \quad \text{in } \Omega \tag{4}$$

where $\boldsymbol{I}$ is the identity tensor. Symbols μ and λ are Lamé constants which are related to the Young's modulus E and Poisson ratio v by

$$\mu = \frac{E}{2\,(1+v)}, \quad \lambda = \frac{vE}{(1+v)\,(1-2v)} \tag{5}$$

The infinitesimal strain tensor ε is defined as a function of the displacement $\boldsymbol{u}$ by

$$\varepsilon\,(\boldsymbol{u}) = \frac{1}{2}\left[\nabla\boldsymbol{u} + (\nabla\boldsymbol{u})^T\right] \tag{6}$$

For simplicity we consider the pure Dirichlet boundary condition ($\Gamma_g = \Gamma$) with $\Gamma_g = 0$. With the notation $\boldsymbol{H}^1\,(\Omega) = \left(H^1\,(\Omega)\right)^2$, the appropriate displacement space for a variational formulation is the Sobolev space $\boldsymbol{H}_0^1\left(\Omega, \Gamma_g\right) := \left\{\boldsymbol{v} \in \boldsymbol{H}^1\,(\Omega) : \boldsymbol{v} = \boldsymbol{0} \text{ on } \Gamma_g\right\}$. In addition to the displacement space, a space of pressure $\mathcal{P}$ is needed. The functions in $\mathcal{P}$ are required to be square-integrable (i.e., L^2-function). We also define a space $L_0^2\,(\Omega)$ to be the subspace of functions in L^2 with zero mean; that is $L_0^2\,(\Omega) = \left\{q \in L^2\,(\Omega),\ \int_\Omega q\,d\Omega = 0\right\}$ under the pure Dirichlet boundary condition assumption. A standard lower-order finite element discretization of domain Ω is based on the conforming space $\boldsymbol{\mathcal{V}}^h$ of continuous piecewise linear approximation on the triangular T^h or bilinear approximation on the quadrilateral Q^h. The corresponding discrete mixed variational problem consists in finding $\boldsymbol{u}^h \in \boldsymbol{\mathcal{V}}^h \subset \boldsymbol{H}_0^1$ and $p^h \in \mathcal{P}^h \subset L_0^2$ such that

$$(M_h)\ \begin{cases} a\left(\boldsymbol{u}^h, \boldsymbol{v}^h\right) + b\left(p^h, \boldsymbol{v}^h\right) = l\left(\boldsymbol{v}^h\right) & \forall\, \boldsymbol{v}^h \in \boldsymbol{\mathcal{V}}^h \\ b\left(q^h, \boldsymbol{u}^h\right) - \frac{1}{\lambda}c\left(p^h, q^h\right) = 0 & \forall\, q^h \in \boldsymbol{\mathcal{P}}^h \end{cases} \tag{7}$$

where

$$\begin{aligned} a\left(\boldsymbol{u}^h, \boldsymbol{v}^h\right) &= 2\mu \int_\Omega \varepsilon\left(\boldsymbol{u}^h\right) : \varepsilon\left(\boldsymbol{v}^h\right) d\Omega \\ b\,(r, \boldsymbol{s}) &= \int_\Omega r\ div(\boldsymbol{s}) d\Omega \\ c\left(p^h, q^h\right) &= \int_\Omega p^h q^h d\Omega \\ l\left(\boldsymbol{v}^h\right) &= \int_\Omega \boldsymbol{b}^T \boldsymbol{v}^h d\Omega \end{aligned} \tag{8}$$

Note that the problem (M_h) is similar to the penalized finite element Stokes problem in [30]. From the Brezzi theorem [11], if the following three conditions are met:

(i) the symmetric bilinear form $a\,(\cdot,\cdot)$ is coercive on kernel space of $b\,(\cdot,\cdot)$:

$\exists$ a constant $\alpha > 0$ such that

$$\begin{aligned} a\left(\boldsymbol{v}^h, \boldsymbol{v}^h\right) &\geq \alpha \left\|\boldsymbol{v}^h\right\|_1^2 \text{ for all } \boldsymbol{v}^h \in Ker\ B^h \\ &= \left\{\boldsymbol{v}^h \in \boldsymbol{\mathcal{V}}^h : b\left(q^h, \boldsymbol{v}^h\right) = 0\ \forall q^h \in \mathcal{P}^h\right\} \end{aligned} \tag{9}$$

(ii) the bilinear form $b\,(\cdot,\cdot)$ satisfies the Inf-sup or LBB (Ladyzenskya–Babuška–Brezzi) condition:

$\exists$ a constant $\beta > 0$ independent of mesh size h such that

$$\inf_{q^h \in \mathcal{P}^h} \sup_{v^h \in \boldsymbol{\mathcal{V}}^h} \frac{b\left(q^h, \boldsymbol{v}^h\right)}{\left\|\boldsymbol{v}^h\right\|_1 \left\|q^h\right\|_0} = \beta_h \geq \beta \tag{10}$$

(iii) the symmetric bilinear form $c\,(\cdot,\cdot)$ is continuous and positive semi-definite:

$$c\left(q^h, q^h\right) \geq 0\ \forall q^h \in \mathcal{P}^h, \tag{11}$$

then the problem (M_h) admits a unique solution for $\left(\boldsymbol{u}^h, p^h\right)$ $\in \boldsymbol{\mathcal{V}}^h \times \mathcal{P}^h$ which is stable and optimally convergent, i.e., there exists a positive constant $C_{\alpha\beta}$ depending on α and β but independent of mesh size h such that

$$\begin{aligned} &\left\|\boldsymbol{u} - \boldsymbol{u}^h\right\|_1 + \left\|p - p^h\right\|_0 \\ &\leq C_{\alpha\beta} \inf_{v^h \in \boldsymbol{\mathcal{V}}^h, q^h \in \mathcal{P}^h} \left(\left\|\boldsymbol{u} - \boldsymbol{v}^h\right\|_1 + \left\|p - q^h\right\|_0\right) \end{aligned} \tag{12}$$

where the symbol $\|\cdot\|_m$ denotes the Sobolev norm of order m as defined in a standard way. It is trivial to see that bilinear form $c\,(\cdot,\cdot)$ is positive semi-definite. The inf-sup condition however is difficult to prove for practical situations in particular when the element mesh is distorted. For this reason a numerical inf-sup test proposed by Chapelle and Bathe [6] turns to be a very useful tool to predicate the stability of a mixed formulation in engineering practice. Given a finite element discretization, the inf-sup condition in inequality (10) can be re-expressed in matrix form

$$\inf_{P^h} \sup_{V^h} \frac{\boldsymbol{P}^{h^T} \boldsymbol{G}^h \boldsymbol{V}^h}{\sqrt{\boldsymbol{V}^{h^T} \boldsymbol{S}^h \boldsymbol{V}^h}\sqrt{\boldsymbol{P}^{h^T} \boldsymbol{G}^h \boldsymbol{P}^h}} = \beta_h \geq \beta \tag{13}$$

where

$$\left\|\boldsymbol{v}^h\right\|_1^2 = \boldsymbol{V}^{h^T} \boldsymbol{S}^h \boldsymbol{V}^h \tag{14}$$

$$\left\|q^h\right\|_0^2 = \boldsymbol{P}^{h^T} \boldsymbol{G}^h \boldsymbol{P}^h \tag{15}$$

$\boldsymbol{V}^h$ and $\boldsymbol{P}^h$ are vectors of the nodal displacement values corresponding to $\boldsymbol{v}^h$ and q^h, and $\boldsymbol{S}^h, \boldsymbol{G}^h$ are matrices defined

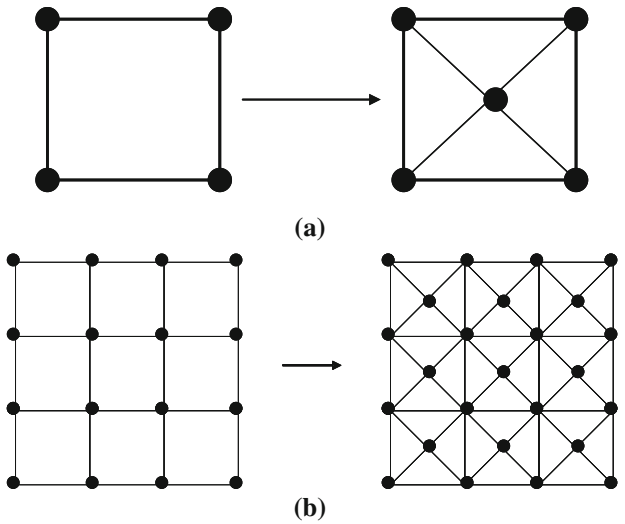

Fig. 1 Crisscross-refinements of quadrilateral elements. **a** Refinement on one quadrilateral element. **b** Refinement on multiple quadrilateral elements

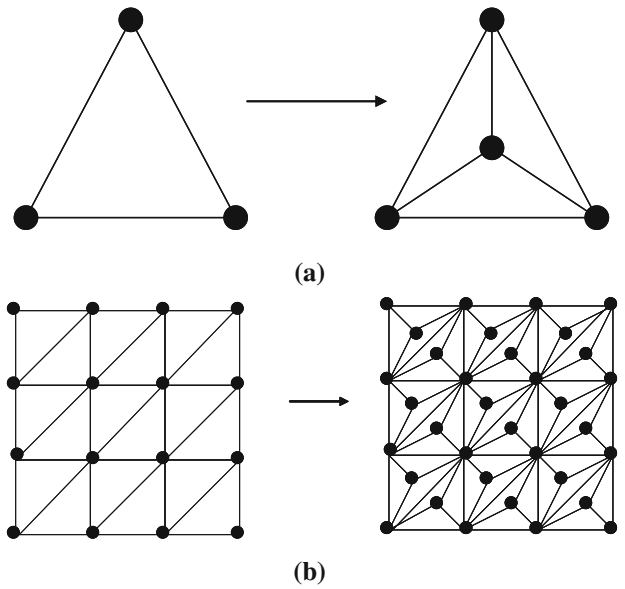

Fig. 2 Hsieh–Clough–Tocher refinements of triangular elements. **a** Refinement on one triangular element. **b** Refinement on multiple triangular elements

according to the Eqs. 14 and 15. If λ_k is the smallest eigenvalue of the following eigenvalue problem

$$\boldsymbol{G}^h \boldsymbol{\varphi} = \lambda \boldsymbol{S}^h \boldsymbol{\varphi}, \tag{16}$$

then the value $\sqrt{\lambda_k}$ is equal to the inf-sup value β_h in Eq. 13 (see, e.g, Bathe [6] for details).

When the domain is discretized using quadrilateral elements $M^h = \cup_e Q^h$, we can eliminate the pressure on the element level by static condensation and obtain a displacement-based formulation as

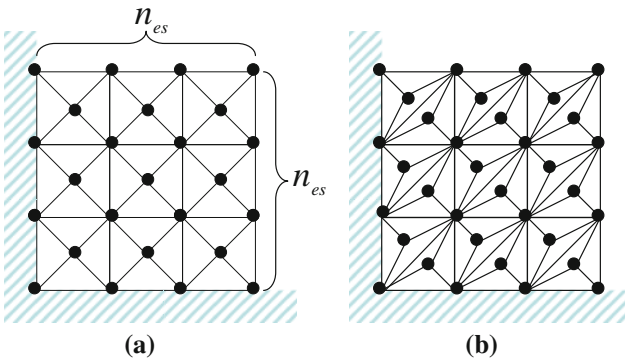

Fig. 3 Standard mesh for constraint ratio counts in the first-level mesh re-partitioning. **a** Crisscross-refined mesh. **b** Hsieh–Clough–Tocher-refined mesh

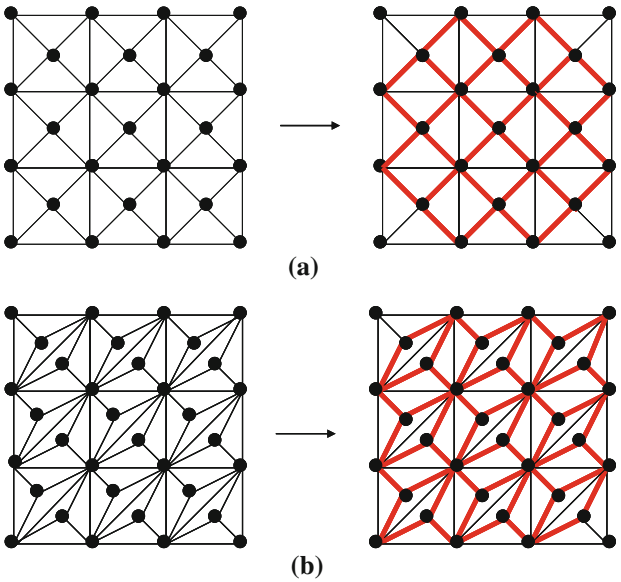

Fig. 4 Multiple strain smoothing domains (in *thick lines*) in **a** Crisscross-refined mesh **b** Hsieh–Clough–Tocher-refined mesh

$$\begin{aligned}(D_h)\ & \int_\Omega 2\mu \boldsymbol{\varepsilon}\left(\boldsymbol{u}^h\right) : \boldsymbol{\varepsilon}\left(\boldsymbol{v}^h\right) d\Omega \\ & + \int_\Omega \lambda \Pi_{\mathcal{P}^h} div\, \boldsymbol{u}^h \Pi_{\mathcal{P}^h} div\, \boldsymbol{v}^h d\Omega \\ & = l\left(\boldsymbol{v}^h\right) \quad \forall\, \boldsymbol{v}^h \in \boldsymbol{\mathcal{V}}^h \end{aligned} \tag{17}$$

where $\Pi_{\mathcal{P}^h}$ denotes a L^2-pojection onto pressure space $\mathcal{P}^h$. Let $P_n\left(Q^h\right)$ denote the polynomials with degree less than or equal to n defined on the quadrilateral element. It is well-known that the chosen pressure space of $\Pi_{\mathcal{P}^h}\mathcal{P}^h = \left\{q \in L_0^2(\Omega)\ \ q|_{Q^h} \in P_0\left(Q^h\right), Q^h \in M^h\right\}$ in $Q_1 - P_0$ mixed element, which corresponds to the reduced/selective integration in bilinear element [29], does not yield a uniform inf-sup condition. For example, the inf-sup value of a uniform mesh

with rectangular elements is of order h^2 : $\beta_h = O\left(h^2\right)$ [30] under homogeneous Dirichlet boundary condition and checkerboard modes in the pressure field might be observed. On the other hand, although $P_1 - P_0$ mixed element (continuous piecewise linear for displacement and piecewise constant for pressure) does provide "consistent" approximations (the range of the divergence is a piecewise constant space as same as the pressure space) for displacement and pressure fields, this element is a locking element. $P_1 - P_0$ mixed element in general does not satisfy the inf-sup condition and therefore is not applicable in practice.

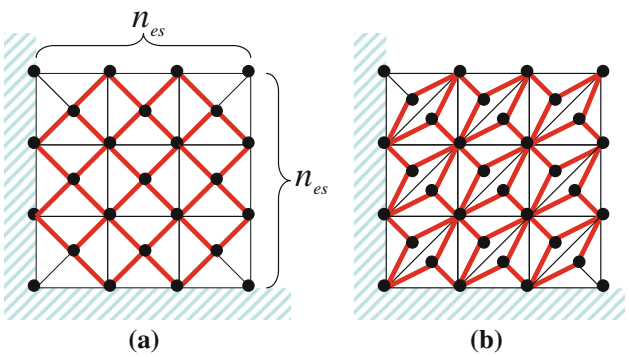

Fig. 5 Standard mesh for constraint ratio counts in the second-level mesh repartitioning with strain smoothing domain (in *thick lines*). **a** Crisscross-refined mesh. **b** Hsieh–Clough–Tocher-refined mesh

3 A two-level mesh repartitioning scheme in linear analysis of nearly incompressible problem

In this section, we present a stable two-level mesh repartitioning scheme for the mixed lower-order finite element method originally discretized either by $Q_1 - P_0$ or $P_1 - P_0$ mixed elements in the solving of nearly incompressible problems. The central idea behind the two-level mesh repartitioning scheme is motivated by the element-wise meshfree enrichments and area-weighted strain smoothing technique in the meshfree-enriched finite element method [42]. In order to define a strain smoothing zone in the finite element method, we first require a refined mesh which is constructed using an h-adaptive mesh refinement scheme in the first-level mesh repartitioning. In the second-level mesh repartitioning, we apply the area-weighted strain smoothing technique [42] leading to a mesh coarsening effect on the first-level refined mesh. Finally, a degeneration of the mixed finite element formulation to a displacement-based finite element formulation based on the repartitioned mesh is presented. Extensions of this approach to nonlinear problems are presented in Sect. 4

3.1 First-level mesh repartitioning: an h-adaptive mesh refinement scheme

Given a quadrilateral partition of a polygonal domain Ω denoted by $M^h = \cup_e Q^h$, an h-adaptive refinement of M^h is defined by $M^{h/2}$ where each quadrilateral $Q^h \in M^h$ is refined by a crisscross-refinement to form four congruent sub-triangles. For convenience, we denote each sub-triangle by $T^{h/2}$. The triangular subdivision of one quadrilateral element $Q^h = \overset{4}{\cup} T^{h/2}$ is shown in Fig. 1a. Figure 1b shows the triangular subdivision on multiple quadrilateral elements. In mixed formulation, the corresponding element $T^{h/2}$ on triangular subdivision is approximated by the $P_1 - P_0$ mixed element where the approximation spaces are defined by

$$\boldsymbol{V}^h = \left\{ \boldsymbol{v}^h \in \boldsymbol{H}_0^1(\Omega) \;\; \boldsymbol{v}^h\big|_{T^h} \in P_1\left(T^{h/2}\right) \;\forall\, T^{h/2} \in M^{h/2} \right\} \tag{18}$$

$$\mathcal{P}^h = \left\{ q \in L_0^2(\Omega) \;\; q|_{T^h} \in P_0\left(T^{h/2}\right), \forall\, T^{h/2} \in M^{h/2} \right\} \tag{19}$$

The h-adaptive mesh refinement in quadrilateral discretization can be applied to triangular discretization $M^h = \cup_e T^h$ leading to a mesh partition similar to the Hsieh–Clough–Tocher [11] mesh. The mesh refinements in single triangular element and multiple elements are depicted in Fig. 2a, b respectively. Since the partitioned sub-triangular elements are also $P_1 - P_0$ mixed elements, their mixed finite element spaces can be defined as in Eqs. 18 and 19.

The resulting mesh from the h-adaptive mesh refinement is composed of $P_1 - P_0$ mixed elements and remains conforming in the displacement approximation. As the divergence of displacement field in $P_1 - P_0$ mixed element is piecewise constant, it leads to a divergence-free finite element space

$$\boldsymbol{Z}^h = \left\{ \boldsymbol{v}^h \in \boldsymbol{\mathcal{V}}^h \,\middle|\, div\, \boldsymbol{v}^h = 0 \right\} \tag{20}$$

Although the $P_1 - P_0$ mixed element provides a discrete divergence-free approximation, it is known that $P_1 - P_0$ mixed element does not work well for a general mesh since the dimension of the discrete displacement space is always less than that of the pressure space, i.e.

$$\dim \boldsymbol{\mathcal{V}}^h < \dim \mathcal{P}^h, \tag{21}$$

and a volumetric locking is likely to occur. In the incompressible limit, the worst case leads to the discrete divergence-free function to become $\boldsymbol{v}^h \in Ker\, \boldsymbol{B}^h = \{0\}$. The over-constrained displacement dimension and thus volumetric locking can be predicted by a heuristic constraint ratio approach introduced by Hughes [21]. Note that the constraint

ratio approach is not served as a stability criterion for the proposed method. The stability of the proposed method will be examined thereinafter by three conditions in inequalities (9–11). The constraint ratio of $P_1 - P_0$ mixed element in a standard crisscross-refined mesh with a number of elements per side n_{es} as shown in Fig. 3a is

$$r = \frac{n_{eq}}{n_c} = 1 \tag{22}$$

where n_{eq} represent the total number of displacement equations after boundary conditions have been imposed and n_c represent the total number of incompressibility constraints.

The constraint ratio in the Hsieh–Clough–Tocher refined mesh shown in Fig. 3b is the same as the one in the crisscross-refined mesh and the ratio does not change when the mesh is refined. Note that the optimal value of constraint ratio r for the volumetric locking-free mesh is two as n_{es} approaches infinity in two-dimensional case. In this study, we increase the constraint ratio of $P_1 - P_0$ mixed elements generated in the first-level refined mesh by spanning the pressure space over the adjacent element. This is done by a second-level mesh coarsening scheme through a strain smoothing technique.

3.2 Second-level mesh repartitioning: a strain smoothing scheme

We recall M^h is an admissible subdivision of computational domain Ω into non-overlapping quadrilateral or triangular element domains. In other words, two elements from M^h either have no intersection, or have a common vertex, or a common edge. Let the symbol l denotes a common edge of adjacent elements $Q^h_{l,j}$, $j = 1, 2$ in the original discretization M^h. The edge l is also a common edge of adjacent elements $T^{h/2}_{l,j}$, $j = 1, 2$ in the refined mesh $M^{h/2}$. The smoothing domain Ω_l corresponding to the edge l for the pair of adjacent elements $T^{h/2}_{l,j}$, $j = 1, 2$ in $M^{h/2}$ is defined as $\Omega_l = \overset{2}{\cup}_{T^{h/2} \in T^{h/2}_l} T^{h/2}$ and the smoothed strain [14,42] is defined by

$$\overline{\boldsymbol{\varepsilon}}^h = \boldsymbol{\Pi}_h \left(\boldsymbol{\varepsilon} \left(\boldsymbol{u}^h \right) \right) = \frac{1}{A_l} \int_{\Omega_l} \boldsymbol{\varepsilon} \left(\boldsymbol{u}^h \right) \Phi_l \left(\boldsymbol{X} \right) d\Omega \tag{23}$$

where $\boldsymbol{\Pi}_h$ denotes the smoothing operator. A_l is the area of the smoothing domain Ω_l. $\Phi_l(\boldsymbol{X})$ is the characteristic or smoothing function of the smoothing domain Ω_l defined by

$$\Phi_l \left(\boldsymbol{X} \right) = \begin{cases} 1, & \text{if } \boldsymbol{X} \in \Omega_l \\ 0, & \text{else} \end{cases} \tag{24}$$

Subsequently, in the second-level mesh re-partitioning we can define a new subdivision of computational domain by $\overline{M}^{h/2} = \cup_l \Omega_l + \cup_b T^{h/2}_b$ where $T^{h/2}_b$ denotes the first-level sub-triangle $T^{h/2}$ whose element edge m contains a piecewise b of global boundary $\partial\Omega = \cup_b m_b$. Since $T^{h/2}_b$ does not share common edge l defined in the original discretization M^h with any adjacent T^h, strain smoothing is not performed on those elements. An exemplary sketch of strain smoothing in the second-level repartitioned mesh is given in Fig. 4a, b for Crisscross refinements and Hsieh–Clough–Tocher refinements respectively.

Subsequently, a smoothed strain gradient matrix $\overline{\boldsymbol{B}}_I$ is defined through the following equation

$$\overline{\boldsymbol{\varepsilon}}^h = \sum_{I=1}^{NP} \overline{\boldsymbol{B}}_I \boldsymbol{u}^h_I \tag{25}$$

and

$$\boldsymbol{u}^h \left(\boldsymbol{X} \right) = \sum_{I=1}^{3} \Psi_I \left(\boldsymbol{X} \right) \boldsymbol{u}_I \tag{26}$$

where $NP = 4$ is the number of nodes involving in each smoothing domain Ω_l. Ψ_I is the linear finite element shape function of node I. The smoothed gradient matrix under plain strain assumption is given by

$$\overline{\boldsymbol{B}}_I = \frac{1}{A_l} \begin{bmatrix} \int_{\Omega_m} \left(\frac{\partial \Psi_I}{\partial X_1} \right) \Phi_l(\boldsymbol{X}) d\Omega & 0 \\ 0 & \int_{\Omega_m} \left(\frac{\partial \Psi_I}{\partial X_2} \right) \Phi_l(\boldsymbol{X}) d\Omega \\ \int_{\Omega_m} \left(\frac{\partial \Psi_I}{\partial X_2} \right) \Phi_l(\boldsymbol{X}) d\Omega & 0 \\ 0 & \int_{\Omega_m} \left(\frac{\partial \Psi_I}{\partial X_1} \right) \Phi_l(\boldsymbol{X}) d\Omega \end{bmatrix} \tag{27}$$

For the simple expression of the equations, we also denote the strain $\boldsymbol{\varepsilon}^h$ in each $T^{h/2}_b$ to be $\overline{\boldsymbol{\varepsilon}}^h$ due to the fact that strain smoothing plays no role for a single linear element, i.e.,

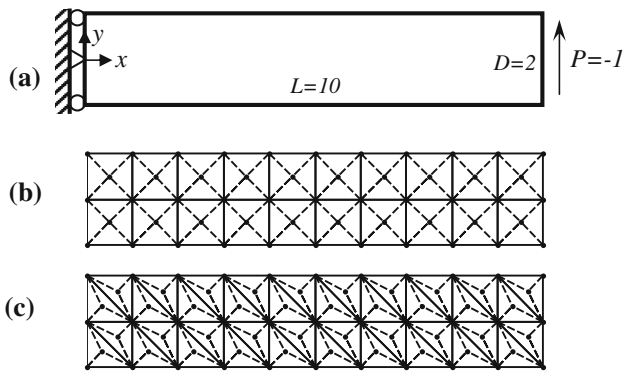

Fig. 6 Cantilever beam

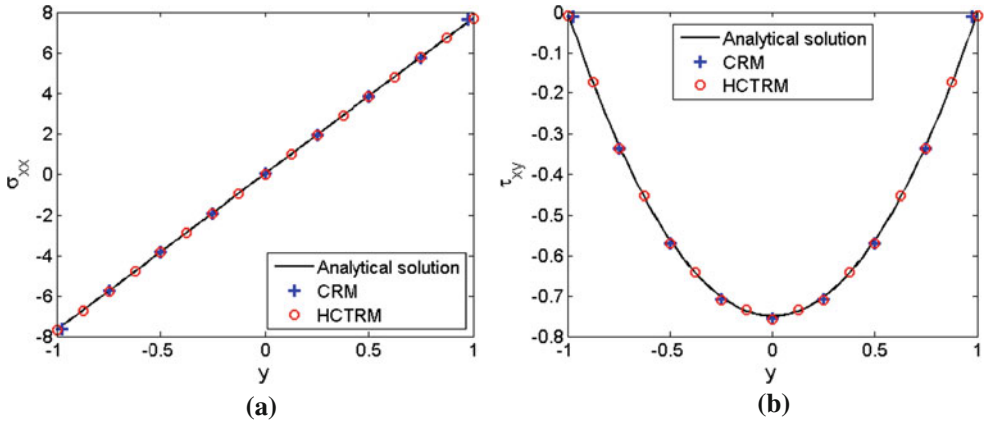

Fig. 7 Stress results along the cross-section $x = 4.875$. **a** σ_{xx} Component. **b** τ_{xy} Component

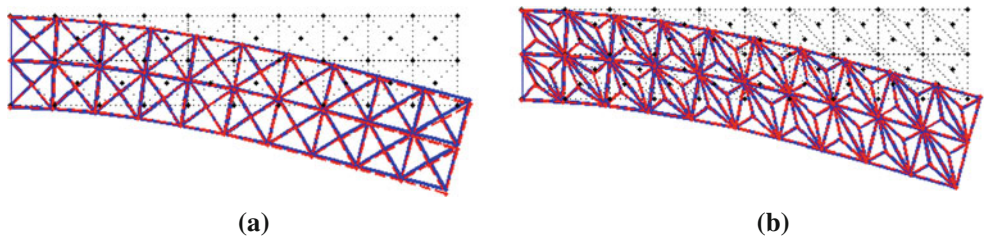

Fig. 8 Deformation plot in nearly-incompressible case (scaled by 5 times): initial (*dash lines*); analytical (*thick red lines*); numerical (*thick blue lines*). **a** CRM. **b** HCTRM. (Color figure online)

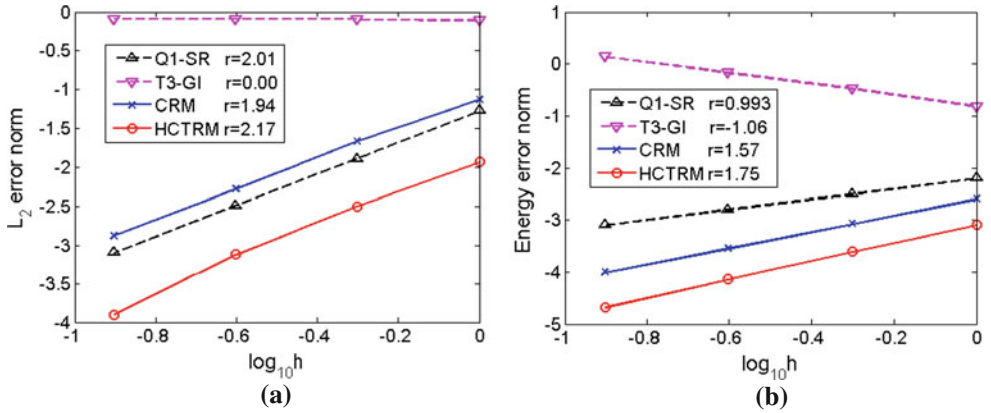

Fig. 9 Convergence of error norms. **a** L_2 Error norm. **b** Energy error norm

$$\overline{\boldsymbol{\varepsilon}}^h\left(\boldsymbol{u}^h\right) = \boldsymbol{\Pi}_h\left(\boldsymbol{\varepsilon}\left(\boldsymbol{u}^h\right)\right) = \frac{1}{A_b}\int\limits_{T_b^{h/2}} \boldsymbol{\varepsilon}\left(\boldsymbol{u}^h\right)\Phi_l\left(\boldsymbol{X}\right)d\Omega$$
$$= \frac{1}{A_l}\int\limits_{\Omega_l} \boldsymbol{\varepsilon}\left(\boldsymbol{u}^h\right)\Phi_l\left(\boldsymbol{X}\right)d\Omega = \boldsymbol{\varepsilon}\left(\boldsymbol{u}^h\right) \tag{28}$$

where A_b is element area of $T_b^{h/2}$. Now we further denote $\overline{M}^{h/2} = \cup_l \Omega_l$.

With the new partitioned mesh and smoothed strain, we can rewrite the discrete problem (M^h) in Eqs. 7 and 8 to be: finding $\boldsymbol{u}^h \in \boldsymbol{\mathcal{V}}^h \subset \boldsymbol{H}_0^1$ and $p^h \in \mathcal{P}^h \subset L_0^2$ such that

$$(\overline{M}_h)\ \begin{cases} \overline{a}\left(\boldsymbol{u}^h, \boldsymbol{v}^h\right) + \overline{b}\left(p^h, \boldsymbol{v}^h\right) = l\left(\boldsymbol{v}^h\right) & \forall\, \boldsymbol{v}^h \in \boldsymbol{\mathcal{V}}^h \\ \overline{b}\left(q^h, \boldsymbol{u}^h\right) - \frac{1}{\lambda}c\left(p^h, q^h\right) = 0 & \forall\, q^h \in \mathcal{P}^h \end{cases} \tag{29}$$

where

$$\overline{a}\left(\boldsymbol{u}^h, \boldsymbol{v}^h\right) = 2\mu\int\limits_{\Omega} \overline{\boldsymbol{\varepsilon}}\left(\boldsymbol{u}^h\right) : \overline{\boldsymbol{\varepsilon}}\left(\boldsymbol{v}^h\right)d\Omega$$
$$\overline{b}\left(r, \boldsymbol{s}\right) = \int\limits_{\Omega} r\ \overline{div}(\boldsymbol{s})d\Omega$$
$$\overline{div}(\boldsymbol{s}) = tr\boldsymbol{\Pi}_h\left(\boldsymbol{\varepsilon}\left(\boldsymbol{s}\right)\right)$$

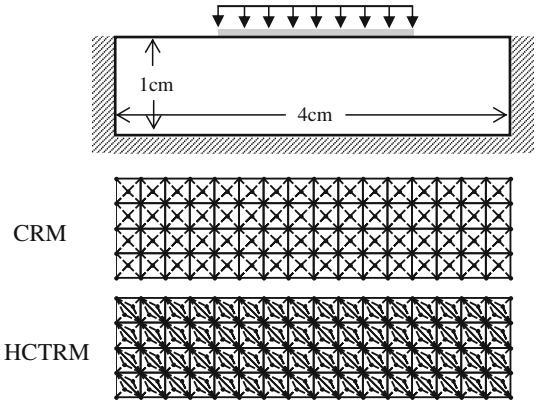

Fig. 10 Geometry, boundary condition and discretization in punch problem

$$c\left(p^h, q^h\right) = \int_\Omega p^h q^h d\Omega$$
$$l\left(\boldsymbol{v}^h\right) = \int_\Omega \boldsymbol{b}^T \boldsymbol{v}^h d\Omega \tag{30}$$

and pressure space $\mathcal{P}^h$ is defined by

$$\mathcal{P}^h = \left\{ q \in L_0^2(\Omega) \;\; q|_{\Omega_l} \in P_0(\Omega_l), \forall\, \Omega_l \in \overline{M}^{h/2} \right\} \tag{31}$$

which contains piecewise constant in each smoothing domain. The discrete problem $\left(\overline{M}_h\right)$ remains subjected to the stability requirements similar to the ones in Eqs. 9 and 10.

Now we are interested in the values of constraint ratio r in the second-level re-partitioned mesh as the number of elements per side, n_{es}, approaches infinity. Figure 5a shows the crisscross-refined mesh after strain smoothing whereas the constraint ratio r becomes

$$r = \lim_{n_{es}\to\infty} \frac{(2n_{es})^2}{2n_{es}^2 + 2n_{es}} = 2 \tag{32}$$

Similarly, the constrain ratio in the Hsieh–Clough–Tocher-refined mesh shown in Fig. 5b can be obtained by

$$r = \lim_{n_{es}\to\infty} \frac{6n_{es}^2}{3n_{es}^2 + 2n_{es}} = 2 \tag{33}$$

In both cases the constraint ratio has been improved to the optimal value. As a result optimal behavior is indicated and volumetric locking-free result is anticipated in the two dimensional nearly incompressible problems.

3.3 A degeneration to displacement-based finite element formulation

Since the pressure p^h is piecewise constant in each smoothing domain Ω_l, we have the first equation in problem $\left(\overline{M}_h\right)$ to be rewritten as

$$2\mu \int_\Omega \overline{\boldsymbol{\varepsilon}}\left(\boldsymbol{u}^h\right) : \overline{\boldsymbol{\varepsilon}}\left(\boldsymbol{v}^h\right) d\Omega + \int_\Omega p^h \left(\overline{div}\; v^h\right) d\Omega$$
$$= \int_\Omega \boldsymbol{b}^T \boldsymbol{v}^h d\Omega = 2\mu \int_\Omega \overline{\boldsymbol{\varepsilon}}\left(\boldsymbol{u}^h\right) : \overline{\boldsymbol{\varepsilon}}\left(\boldsymbol{v}^h\right) d\Omega$$
$$+ \sum_{l=1}^{nl} \left(\frac{1}{A_l} \int_{\Omega_l} p^h d\Omega \int_{\Omega_l} \overline{div}\; \boldsymbol{v}^h d\Omega \right) \quad \forall \boldsymbol{v}^h \in \boldsymbol{\mathcal{V}}^h \tag{34}$$

where the index nl in Eq. 34 denotes the total number of smoothing domain Ω_l in $\overline{M}^{h/2}$ ($\overline{M}^{h/2} = \overset{nl}{\cup_l}\Omega_l$). The second equation in problem $\left(\overline{M}_h\right)$ reads

$$\int_\Omega q^h \left(\overline{div}\; \boldsymbol{u}^h\right) d\Omega - \frac{1}{\lambda} \int_\Omega p^h q^h d\Omega = 0 \quad \forall q^h \in \mathcal{P}^h \tag{35}$$

Correspondingly, we have

$$\lambda \int_{\Omega_l} \left(\overline{div}\; \boldsymbol{u}^h\right) d\Omega - \int_{\Omega_l} p^h d\Omega = 0 \quad \forall \Omega_l \in \Omega \tag{36}$$

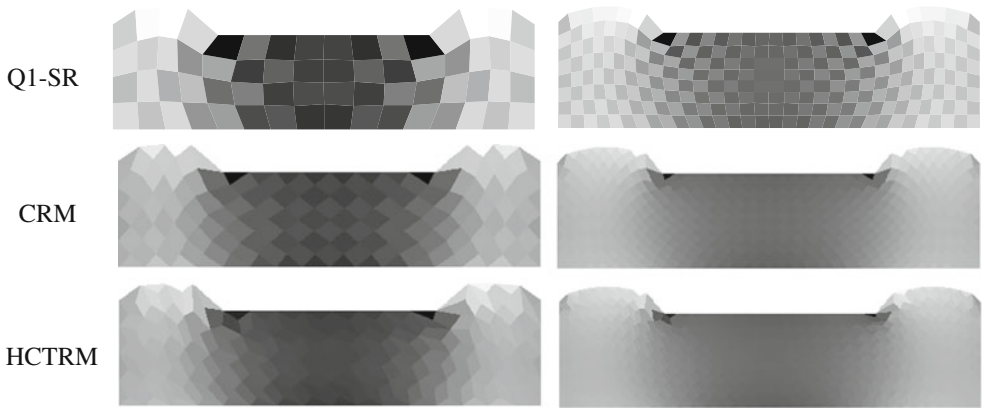

Fig. 11 Pressure distribution of punch problem

Table 1 Convergence of forces on the flat rigid punch in 2D

Elements		Q1-SR	CRM	HCTRM
Q1	Tri			
8×2	32	2146.5615	1862.0769	1679.8587
16×4	128	1637.0067	1507.5453	1473.8086
24×6	288	1521.8001	1439.7286	1423.4289
32×8	512	1472.0337	1412.5224	1401.8695

The combination of Eqs. 34 and 36 yields to

$$
\begin{aligned}
&2\mu\int_{\Omega}\overline{\boldsymbol{\varepsilon}}\left(\boldsymbol{u}^h\right):\overline{\boldsymbol{\varepsilon}}\left(\boldsymbol{v}^h\right)d\Omega+\int_{\Omega}p^h\left(\overline{div}\ v^h\right)d\Omega=\int_{\Omega}\boldsymbol{b}^T\boldsymbol{v}^h d\Omega\\
&=2\mu\int_{\Omega}\overline{\boldsymbol{\varepsilon}}\left(\boldsymbol{u}^h\right):\overline{\boldsymbol{\varepsilon}}\left(\boldsymbol{v}^h\right)d\Omega+\sum_{l=1}^{nl}\left(\frac{1}{A_l}\int_{\Omega_l}p^h d\Omega\int_{\Omega_l}\overline{div}\ \boldsymbol{v}^h d\Omega\right)\\
&=2\mu\int_{\Omega}\overline{\boldsymbol{\varepsilon}}\left(\boldsymbol{u}^h\right):\overline{\boldsymbol{\varepsilon}}\left(\boldsymbol{v}^h\right)d\Omega+\sum_{l=1}^{nl}\left(\frac{\lambda}{A_l}\int_{\Omega_l}\overline{div}\ \boldsymbol{u}^h d\Omega\int_{\Omega_l}\overline{div}\ \boldsymbol{v}^h d\Omega\right)\\
&=2\mu\int_{\Omega}\overline{\boldsymbol{\varepsilon}}\left(\boldsymbol{u}^h\right):\overline{\boldsymbol{\varepsilon}}\left(\boldsymbol{v}^h\right)d\Omega+\lambda\int_{\Omega}\overline{div}\ \boldsymbol{u}^h\ \overline{div}\ \boldsymbol{v}^h d\Omega\ \forall\,\boldsymbol{v}^h\in\boldsymbol{\mathcal{V}}^h
\end{aligned}
\tag{37}
$$

We can rewrite Eq. 37 using the definition of $\boldsymbol{\Pi}_h$ in Eq. 28 leading to the following reduced problem: finding $\boldsymbol{u}^h\in\boldsymbol{\mathcal{V}}^h\subset\boldsymbol{H}_0^1$ such that

$$
\left(\overline{D}_h\right)\ \overline{\boldsymbol{A}}\left(\boldsymbol{u}^h,\ \boldsymbol{v}^h\right)\ =l\left(\boldsymbol{v}^h\right)\ \forall\,\boldsymbol{v}^h\in\boldsymbol{\mathcal{V}}^h \tag{38}
$$

where

$$
\overline{\boldsymbol{A}}\left(\boldsymbol{u}^h,\boldsymbol{v}^h\right)\ =\ \int_{\Omega}\boldsymbol{\Pi}_h\boldsymbol{\varepsilon}\left(\boldsymbol{u}^h\right):\boldsymbol{C}\boldsymbol{\Pi}_h\boldsymbol{\varepsilon}\left(\boldsymbol{v}^h\right)d\Omega \tag{39}
$$

Now the reduced problem $\left(\overline{D}_h\right)$ is corresponding to a discretization of the primal problem (pure displacement) in $\boldsymbol{\mathcal{V}}^h$ with a L^2 -orthogonal projection on strains defined in Eq. 28. Although the total number of degrees of freedom is increased after the two-level mesh-repartitioning, the proposed finite element scheme does not need to solve the pressure unknowns. This is because the pressure does not appear explicitly in the formulation, and therefore a static condensation procedure that used in the standard mixed formulation in order to eliminate the pressure unknown is not needed in the current formulation. Although the pressure does not appear explicitly in the displacement-based finite element formulation, the well-posedness of the reduced problem $\left(\overline{D}_h\right)$ in near-incompressible regime is still subject to a stability condition, i.e., the discrete inf-sup conditions between the displacement space $\boldsymbol{\mathcal{V}}^h$ and an implicit pressure space P^h induced by the following equation

$$
p^h=-\lambda\ tr\boldsymbol{\Pi}_h\left(\boldsymbol{\varepsilon}\left(\boldsymbol{u}^h\right)\right)=-\lambda\ \overline{div}\left(\boldsymbol{u}^h\right)\ in\ \mathcal{P}^h \tag{40}
$$

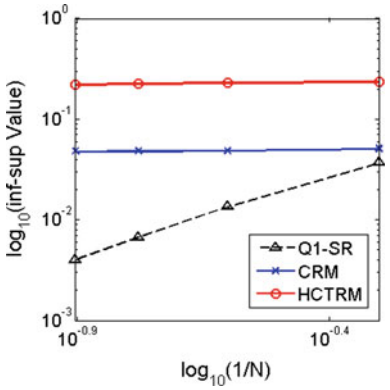

Fig. 12 Numerical inf-sup test result for the punch problem

Same displacement-based finite element formulation can be obtained following from the derivation provided in [42] based on the Hu–Washizu variational principle [40]. The coercivity of bilinear form $\overline{A}(,\cdot,)$ on $\boldsymbol{\mathcal{V}}^h\times\boldsymbol{\mathcal{V}}^h$ in problem $\left(\overline{D}_h\right)$ as well as $\overline{a}(,\cdot,)$ in problem $\left(\overline{M}_h\right)$ can also be shown following from the proof in [42, Theorem 4.3]. Since the consistency between the smoothed divergence space and pressure space in Eq. 40 does not guarantee a stable pair of approximations in displacement and pressure fields, the stability of the proposed finite element scheme is verified in Sect. 5 through the numerical inf-sup test [6] as described in Sect. 2.

4 Nonlinear hyper-elasticity problem

The major interest of the proposed method is in the large deformation analysis of hyper-elastic materials. In this section, we focus on the development of nonlinear version of the proposed method for hyper-elastic materials where the smoothing scheme described in Sect.3.2 is performed on the deformation gradient. In order to introduce the smoothed deformation gradient into Galerkin approximation for the finite strain analysis, the following mixed three-field Hu–Washizu–de Veubeke energy functional [40] is considered for the derivation of nonlinear finite element formulation for hyperelastic materials.

$$
\begin{aligned}
U_{HW}\left(\boldsymbol{u},\overline{\boldsymbol{F}},\overline{\boldsymbol{\tau}}\right)=&\int_{\Omega}W\left(\overline{\boldsymbol{F}}\right)d\Omega+\int_{\Omega}\overline{\boldsymbol{\tau}}:\left(\nabla_0\boldsymbol{u}-\overline{\boldsymbol{F}}\right)d\Omega\\
&-\boldsymbol{W}_{ext}\left(\boldsymbol{u}\right)
\end{aligned}
\tag{41}
$$

where the displacements $\boldsymbol{u}$, smoothed deformation gradient $\overline{\boldsymbol{F}}$ and smoothed first Piola–Kirchhoff stresses $\overline{\boldsymbol{\tau}}$ are independently varied. The symbol ∇_0 denotes the gradient operator with respect to the original configuration. $W=W\left(\overline{\boldsymbol{F}}\right)$ is the assumed strain energy density function. The term W_{ext} designates the external work. The smoothed first Piola–Kirchhoff stresses $\overline{\boldsymbol{\tau}}$ is related to the smoothed deformation gradient $\overline{\boldsymbol{F}}$ by

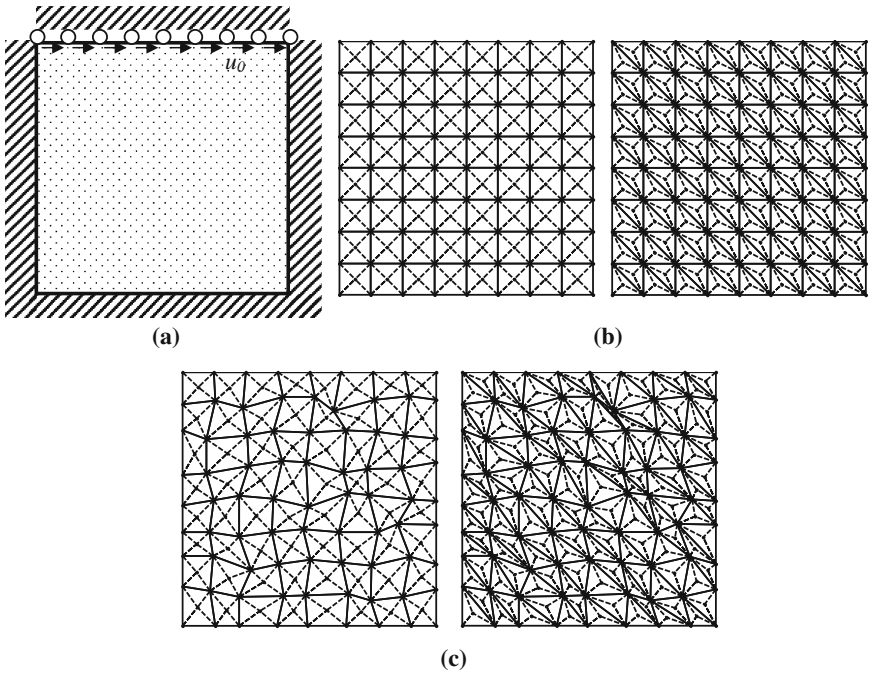

Fig. 13 Driven cavity problem. **a** Geometry and boundary condition. **b** Uniform discretization. **c** Non-uniform discretization

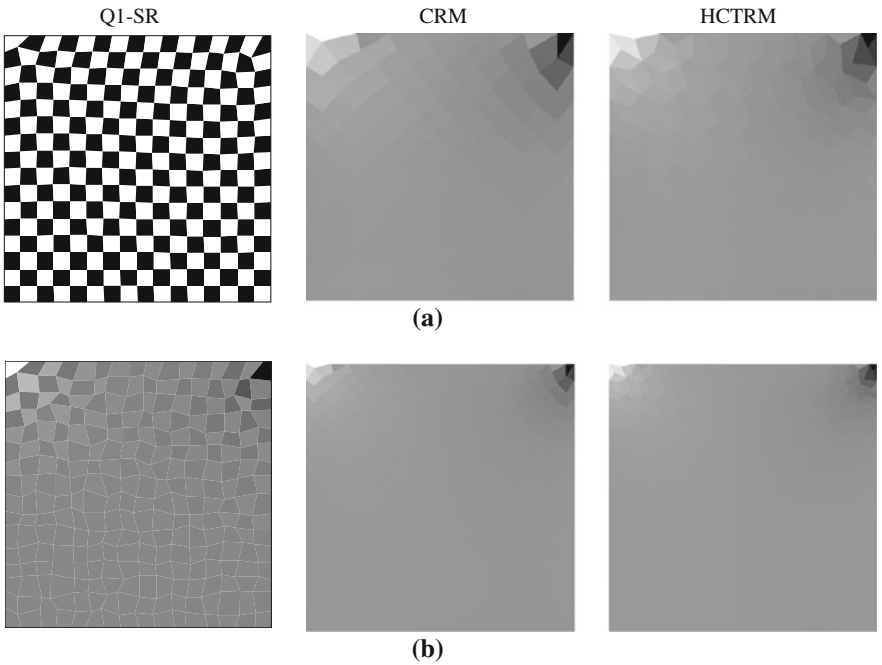

Fig. 14 Pressure distribution of driven cavity problem. **a** Uniform mesh. **b** Non-uniform mesh

$$\overline{\boldsymbol{\tau}} = \frac{\partial W}{\partial \overline{\boldsymbol{F}}} \tag{42}$$

The energy functional in Eq. 41 is taken as a basis for the numerical discretization. The discretization of domain Ω using the two-level mesh repartitioning scheme and standard linear finite element give the following discretized total energy functional:

$$U^h_{HW} : \mathcal{V}^h \times \boldsymbol{\Xi}^h \times \boldsymbol{\Theta}^h \to R$$

$$U^h_{HW}\left(\boldsymbol{u}^h, \overline{\boldsymbol{F}}^h, \overline{\boldsymbol{\tau}}^h\right) = \int_\Omega W\left(\overline{\boldsymbol{F}}^h\right) d\Omega + \int_\Omega \overline{\boldsymbol{\tau}}^h : \left(\nabla_0 \boldsymbol{u}^h - \overline{\boldsymbol{F}}^h\right) d\Omega - W_{ext}\left(\boldsymbol{u}^h\right) \tag{43}$$

where the discrete smoothed deformation gradient $\overline{\boldsymbol{F}}^h$ is defined by

$$\overline{\boldsymbol{F}}^h = \boldsymbol{\Pi}_h\left(\boldsymbol{F}\left(\boldsymbol{u}^h\right)\right) = \frac{1}{A_l}\int_{\Omega_l} \boldsymbol{F}\left(\boldsymbol{u}^h\right)\Phi_l\left(\boldsymbol{X}\right)d\Omega \tag{44}$$

Here, we use the same the notation of smoothing operator "$\boldsymbol{\Pi}_h$" for the smoothing of deformation gradient as we did for the smoothing of strain in linear elasticity problem. A_l denotes the area of the smoothing domain Ω_l. $\Phi_l\left(\boldsymbol{X}\right)$ is defined in Eq. 24. The components of the discrete smoothed deformation gradient is further expressed as

$$\begin{aligned}\overline{F}^h_{ij} &= \frac{1}{A_l}\int_{\Omega_l}\left(\frac{\partial u^h_i}{\partial X_j}+\delta_{ij}\right)\Phi_l\left(\boldsymbol{X}\right)d\Omega \\ &= \frac{1}{A_l}\int_{\Omega_l}\left(\frac{\partial u^h_i}{\partial X_j}\right)\Phi_l\left(\boldsymbol{X}\right)d\Omega+\delta_{ij} \\ &= \frac{1}{A_l}\int_{\Omega_l}\sum_{I=1}^{4}\left(\frac{\partial \Psi_i}{\partial X_j}u_{iI}\right)\Phi_l\left(\boldsymbol{X}\right)d\Omega+\delta_{ij}\equiv \overline{g}^h_{ij}+\delta_{ij}\end{aligned} \tag{45}$$

where

$$\overline{g}^h_{ij} = \frac{1}{A_l}\int_{\Omega_m}\sum_{I=1}^{4}\left(\frac{\partial \Psi_I}{\partial X_j}u_{iI}\right)\Phi_l\left(\boldsymbol{X}\right)d\Omega \tag{46}$$

Since the discrete smoothed deformation gradient is defined locally on each smoothing domain Ω_l and no continuity conditions are applied at the boundaries of Ω_l, the approximation space of smoothed deformation gradient can be defined by

$$\begin{aligned}&\boldsymbol{\Xi}^h\left(\Omega\right) \\ &=\left\{\overline{\boldsymbol{F}}^h : \overline{\boldsymbol{F}}^h \in L^2\left(\Omega\right), \overline{\boldsymbol{F}}^h \text{contains piecewise constants} \,\forall\, \Omega_l \in M_{h/2}\right\}\end{aligned} \tag{47}$$

where the space $\boldsymbol{\Theta}^h \in L^2$ of smoothed first Piola–Kirchhoff stresses also contain piecewise constants in Ω. The second term on the RHS of Eq. 41 can be further expressed using Eq. 44 to yield

$$\begin{aligned}\int_{\Omega}\overline{\boldsymbol{\tau}}^{hT}\left(\nabla_0\boldsymbol{u}^h-\overline{\boldsymbol{F}}^h\right)d\Omega &= \sum_{l=1}^{nl}\overline{\boldsymbol{\tau}}^{hT}\int_{\Omega_l}\left(\nabla_0\boldsymbol{u}^h-\overline{\boldsymbol{F}}^h\right)d\Omega \\ &= \sum_{l=1}^{nl}\overline{\boldsymbol{\tau}}^{hT}\left(\int_{\Omega_l}\nabla_0\boldsymbol{u}^h d\Omega-\overline{\boldsymbol{F}}^h A_l\right) \\ &= \sum_{l=1}^{nl}\overline{\boldsymbol{\tau}}^{hT}\left(\int_{\Omega_l}\nabla_0\boldsymbol{u}^h d\Omega-\int_{\Omega_l}\nabla_0\boldsymbol{u}^h d\Omega\right)=0\end{aligned} \tag{48}$$

Equation 48 implies an orthogonal condition between the discrete stress field $\overline{\boldsymbol{\tau}}^h$ and the difference of the discrete deformation gradient $\nabla_0\boldsymbol{u}^h$ field and the discrete smoothed deformation gradient field $\overline{\boldsymbol{F}}^h$. This is equivalent to the assumed strain variation principle of Simo and Hughes [34].

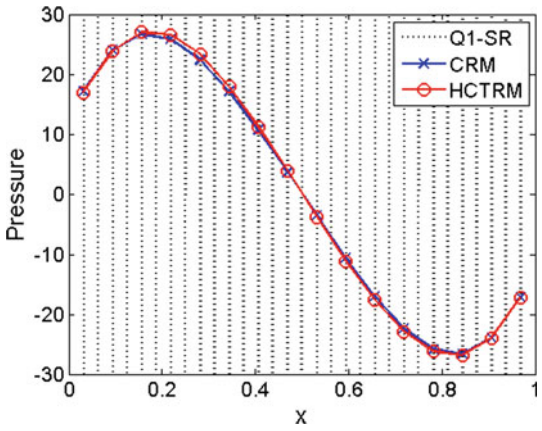

Fig. 15 Pressure distribution at $y = 0.5$

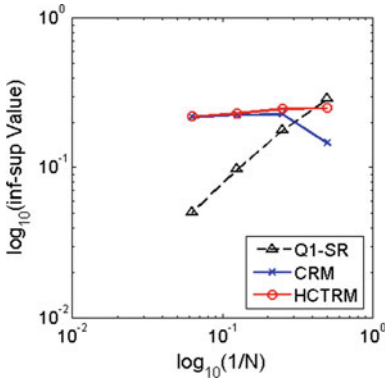

Fig. 16 Numerical inf-sup test result for the cavity problem

After eliminating the stress components from Eq. 41 using Eq. 48, the following modified Hu–Washizu functional is obtained depending only on displacement and smoothed deformation fields:

$$U^h_{HW\ \mathrm{mod}}\left(\boldsymbol{u}^h,\overline{\boldsymbol{F}}^h\right) = \int_{\Omega} W\left(\overline{\boldsymbol{F}}^h\right)d\Omega - W_{ext}\left(\boldsymbol{u}^h\right) \tag{49}$$

The two-field variational problem can be condensed to following primal problem by the definition of Eq. 44:

$$\begin{aligned}\overline{U}^h_{HW\ \mathrm{mod}}\left(\boldsymbol{u}^h\right) &= \int_{\Omega} W\left(\overline{\boldsymbol{F}}^h\left(\boldsymbol{u}^h\right)\right)d\Omega - W_{ext}\left(\boldsymbol{u}^h\right) \\ &= \int_{\Omega} W\left(\boldsymbol{\Pi}_h\boldsymbol{F}^h\left(\boldsymbol{u}^h\right)\right)d\Omega - W_{ext}\left(\boldsymbol{u}^h\right)\end{aligned} \tag{50}$$

Since two variational equations are identical in this study, we choose to work on the two-field variational form for the ease of the following derivation. The approximation solution of the hyper-elasticity problem can be found by finding the stationary points of the two-field variational formulation of

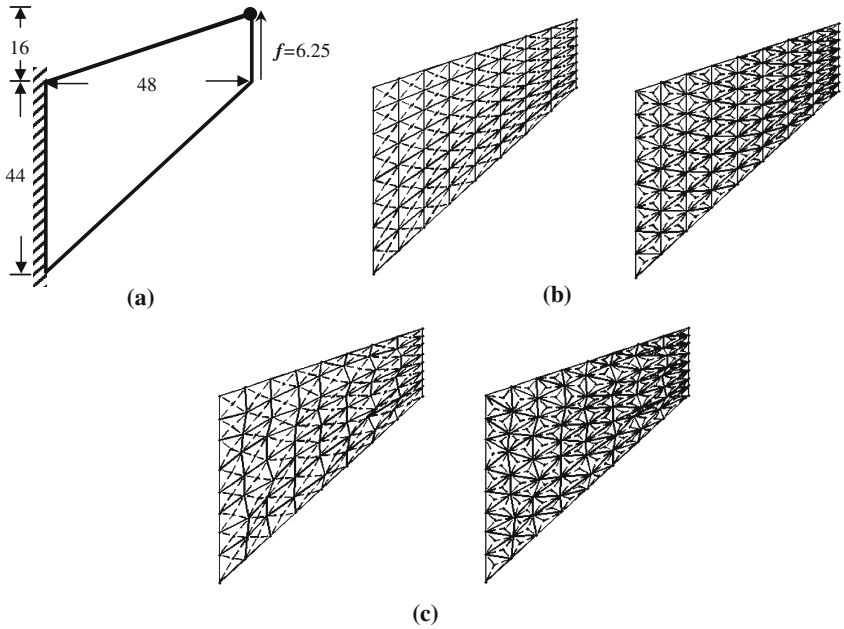

Fig. 17 Cook's membrane problem. **a** Geometry and boundary conditions. **b** Regular discretization. **c** Non-uniform discretization

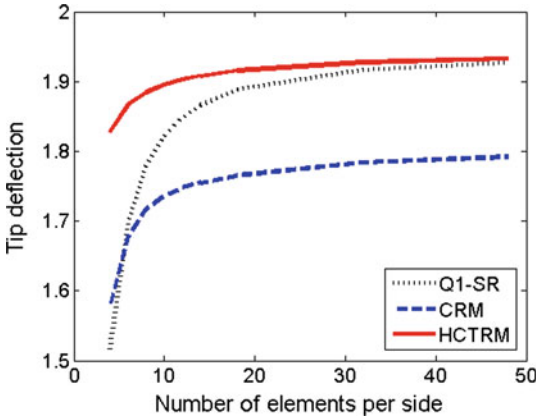

Fig. 18 Tip deflection results for Cook's membrane

Eq. 49 with respect to the variations $\delta \boldsymbol{u}^h$ and $\delta \overline{\boldsymbol{F}}^h$. Since the material frame indifference restricts the dependence of strain energy density function W on smoothed deformation gradient $\overline{\boldsymbol{F}}$, it is advantageous to express the variational equation in terms of the Total Lagrangian formulation. Variation of potential energy in Eq. 49 leads to the following variational equation:

$$\begin{aligned}\delta U^h_{HW\ \mathrm{mod}}\left(\boldsymbol{u}^h, \overline{\boldsymbol{F}}^h\right) &= \int_\Omega \delta \overline{\boldsymbol{F}}^h_{ij} \frac{\partial W\left(\overline{\boldsymbol{F}}^h\right)}{\partial \overline{\boldsymbol{F}}_{ij}} d\Omega - \delta W_{ext}\left(\boldsymbol{u}^h\right) \\ &= \int_\Omega \delta \overline{g}^h_{ij} \overline{\tau}_{ij}\left(\overline{\boldsymbol{F}}^h\right) d\Omega - \delta W_{ext}\left(\boldsymbol{u}^h\right)\end{aligned} \tag{51}$$

where $\overline{g}^h_{ij}$ is defined in Eq. 46.

Now introduce the approximations of displacement in Eq. 26 and smoothed deformation gradient in Eq. 45 into linearization of Eq. 51 together with the numerical integration to yield the following incremental matrix equation for the nonlinear quasi-static analysis

$$\delta \{\boldsymbol{U}\}^T \overline{\boldsymbol{K}}^v_{n+1} \left(\Delta \{\boldsymbol{U}\}\right)^{v+1}_{n+1} = -\delta \{\boldsymbol{U}\}^T \boldsymbol{R}^v_{n+1} \tag{52}$$

where $\{\boldsymbol{U}\}$ is the displacement vector. The tangent stiffness matrix $\boldsymbol{K}^v_{n+1} \left(\Delta \{\boldsymbol{U}\}\right)^{v+1}_{n+1}$ contains the material and geometric stiffness matrices that evaluated at the vth iteration during the $(n+1)$ time incremental step. $\boldsymbol{R}^v_{n+1}$ is the residual nodal force vector. They are given by

$$\overline{\boldsymbol{K}}_{IJ} = \sum_{l=1}^{nl} \sum_{I=1}^{NP} \overline{\boldsymbol{B}}^T_I \left[\overline{\boldsymbol{C}}\left(\overline{\boldsymbol{F}}^h\right) + \overline{\boldsymbol{S}}\left(\overline{\boldsymbol{F}}^h\right)\right] \overline{\boldsymbol{B}}_J A_l \tag{53}$$

$$-\boldsymbol{R} = \boldsymbol{f}^{ext} - \boldsymbol{f}^{int} \tag{54}$$

$$\boldsymbol{f}^{int}_I = \sum_{l=1}^{nl} \sum_{I=1}^{NP} \overline{\boldsymbol{B}}^T_I \overline{\boldsymbol{\tau}}\left(\overline{\boldsymbol{F}}^h\right) A_l \tag{55}$$

$$\boldsymbol{f}^{ext}_I = \int_\Omega \Psi_I \boldsymbol{b}_0 d\Omega + \int_{\Gamma_h} \Psi_I \boldsymbol{h}_0 d\Gamma \tag{56}$$

where smoothed gradient matrix $\overline{\boldsymbol{B}}_I$ is given in Eq. 27, $\overline{\boldsymbol{C}}$ and $\overline{\boldsymbol{S}}$ are the matrices corresponding to material and geometric nonlinearities. Because the smoothed gradient matrix $\overline{\boldsymbol{B}}_I$ is defined in the original configuration, the smoothing procedure described in Sect. 3.2 only needs to be performed at once. The smoothed first Piola–Kirchhoff stresses $\overline{\boldsymbol{\tau}}$ is given in Eq. 42 and is expressed in vector form with its components given by

$$\overline{\boldsymbol{\tau}} = \{\overline{\boldsymbol{\tau}}_{11}, \overline{\boldsymbol{\tau}}_{22}, \overline{\boldsymbol{\tau}}_{12}, \overline{\boldsymbol{\tau}}_{21}\}^T \tag{57}$$

Note that the proposed two-level mesh re-partitioning scheme does not involve a new discretization on the boundary, and therefore the boundary, contact and constraint conditions remain the same as in the original setting. To this end, we have presented the above nonlinear formulation in a way that it can be integrated in a standard displacement-based finite element framework.

5 Numerical examples

In this section, we analyze two-dimensional benchmark examples to study the performance of the two-level repartitioning scheme with both Crisscross-refined mesh (CRM) and Hsieh–Clough–Tocher-refined mesh (HCTRM) for nearly incompressible material in linear and nonlinear analysis. As comparison, we also provide the results using (1) the 4-noded Q1 bilinear element with the selected reduced integration (Q1-SR) (2) the standard 3-noded triangular element with 1-point Gauss integration (T3-GI). Unless otherwise specified, the following material constants are used for all linear benchmark examples: Young's modulus $E = 1000$, Poisson ratio $v = 0.4999999$. The following $\boldsymbol{L}^2$ and energy error norms are used for the investigation of convergence rates:

$$e^h_{\boldsymbol{u}L^2} = \sqrt{\int_\Omega \left[\left(u^h_x - u_x\right)^2 + \left(u^h_x - u_x\right)^2\right] d\Omega}$$
$$e^h_{\boldsymbol{u}E} = \sqrt{\int_\Omega \left[\left(\boldsymbol{\varepsilon}\left(\boldsymbol{u}^h\right) - \boldsymbol{\varepsilon}\left(\boldsymbol{u}\right)\right) : \boldsymbol{C} : \left(\boldsymbol{\varepsilon}\left(\boldsymbol{u}^h\right) - \boldsymbol{\varepsilon}\left(\boldsymbol{u}\right)\right)\right] d\Omega} \tag{58}$$

5.1 Cantilever beam

Consider a cantilever beam problem, as shown in Fig. 6a, in near-incompressible cases. Analytical displacement field is prescribed along $x = 0$, and parabolic vertical traction P is applied along $x = 10$. The analytical displacement and stress solutions are given as [38]:

$$u_x = -\frac{Py}{6\tilde{E}I}\left[(6L-3x)\,x + (2+\tilde{v})\left(y^2 - \frac{D^2}{4}\right)\right]$$
$$u_y = \frac{P}{6\tilde{E}I}\left[3vy^2\,(L-x) + (4+5v)\,\frac{D^2 x}{4} + (3L-x)\,x^2\right],$$
$$\sigma_{xx} = -\frac{P\,(L-x)\,y}{I},\ \sigma_{yy} = 0,\ \sigma_{xy} = \frac{P}{2I}\left(\frac{D^2}{4} - y^2\right) \tag{59}$$

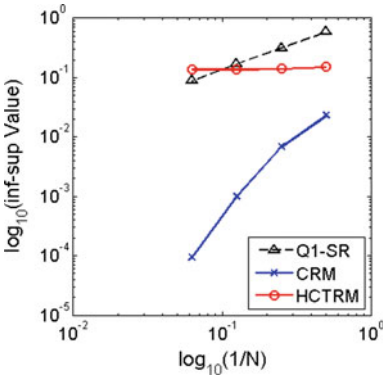

Fig. 20 Numerical inf-sup test result for the Cook's membrane problem

where $\tilde{E} = E/\left(1 - v^2\right)$, $\tilde{v} = v/\left(1 - v\right)$ under plane strain assumption and $I = D^3/12$ is the moment of the inertia of the beam. The computational domain is discretized uniformly with either Crisscross-refined mesh (CRM) or Hsieh–Clough–Tocher-refined mesh (HCTRM) as shown in Fig. 6b, c.

Figure 7a, b depict stress component results of integration points along the cross-section $x = 4.875$ using CRM and HCTRM generated from 40×8 uniform quadrilateral mesh, where the numerical results agree with analytical solution very well.

Superior performance of the proposed two-level mesh repartition scheme is presented in deformation plot (Fig. 8) and convergence of the L_2-norm and energy-norm errors (Fig. 9). The L_2-norm errors of CRM and HCTRM solutions are close to the theoretical asymptotic rate of $O(h^2)$ as shown in Fig. 9a. Higher rate in the energy error norm HCTRM as shown in Fig. 9b. On the other hand, the T3-Gi solution is observed in both CRM and generates a poor rate of $O(h^0)$ in the L_2-norm errors that corresponds to its locking behavior in the near-incompressible analysis. Q1-SR, CRM and HCTRM all pass the numerical inf-sup test in this example.

5.2 Punch problem

The model consists of a block of nearly incompressible material punched by a rigid, frictionless and flat plate with a prescribed displacement. The model geometry and the discretization are shown in Fig. 10. For each numerical method, two uniform meshes are first tested to study the pressure distribution and possible pressure oscillation due to the mesh size effect. The resulting pressure distribution is plotted on the deformed domain and shown in Fig. 11. Although the Q1-SR does not exhibit volumetric locking behavior, visible checkerboard patterns are observed in the pressure field. The

mesh refinement in Q1-SR does not improve the oscillation in the pressure field. Smooth pressure distribution of both CRM and HCTRM shown in Fig. 11 clearly demonstrates their superior performance over Q1-SR. Table 1 summarizes the convergence behavior of the punch force in three methods as mesh is refined. Consistent convergence results are obtained in all three methods.

The numerical inf-sup test is conducted with continuous mesh refinement for the stability study. CRM and HCTRM pass the numerical inf-sup test in which the inf-sup value is independent of the mesh size as shown in Fig. 12. By way of contrast, the inf-sup value computed in Q1-SR differs markedly as it varies and approaches to zero when mesh is continuously refined.

5.3 Driven cavity problem

We consider the problem of a unit square subjected to a unit horizontal displacement along the upper boundary as shown in Fig. 13a. This boundary condition results in corner singularities for the solution for which the exact solution is not known. The aim here is to demonstrate numerically the smoothed pressure solution can be achieved by the proposed approach. The discretizations of CRM and HCTRM are shown in Fig. 13b. Non-uniform discretizations of CRM and HCTRM are also considered in the analysis and are shown in Fig. 13c.

Pressure distributions are plotted on the deformed configuration and shown in Fig. 14. Spurious pressure modes are

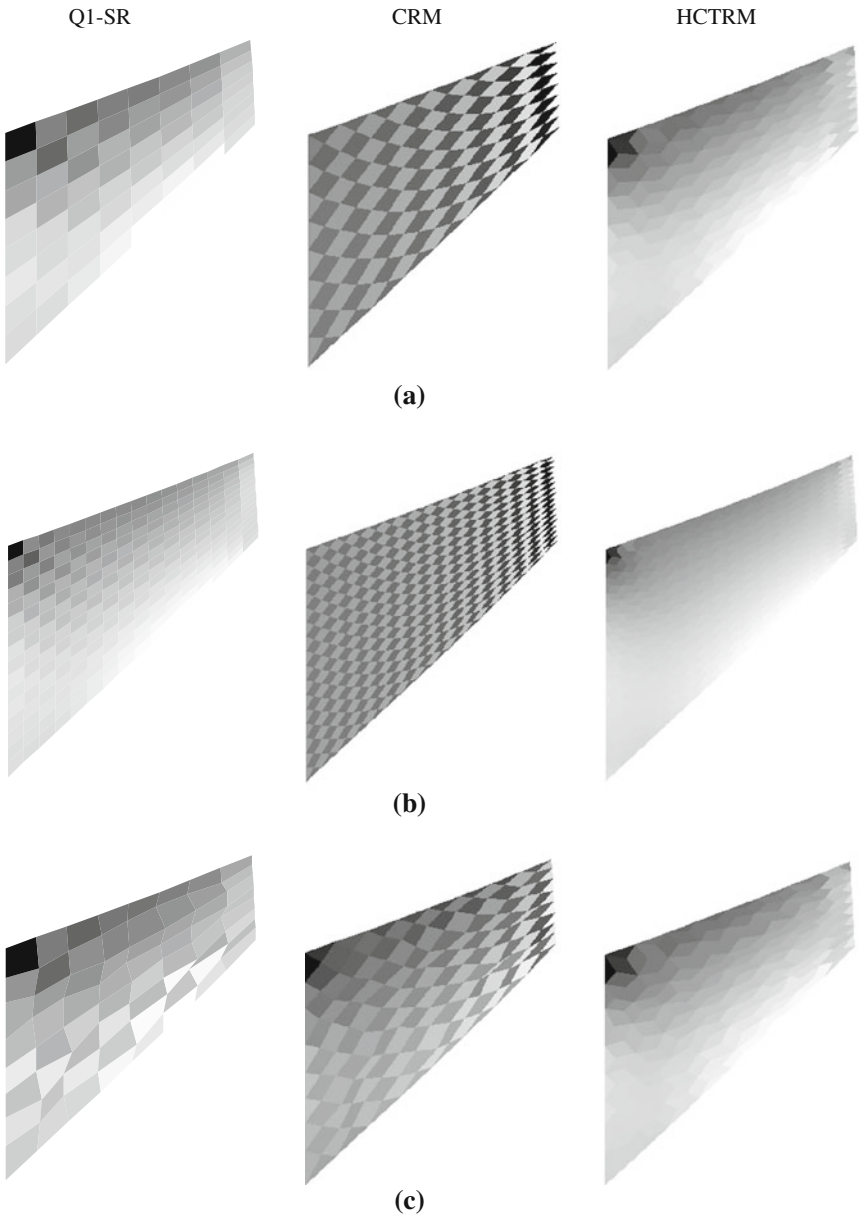

Fig. 19 Pressure distribution of Cook's membrane problem. **a** 8×8 Mesh. **b** 16×16 Mesh. **c** Non-uniform mesh

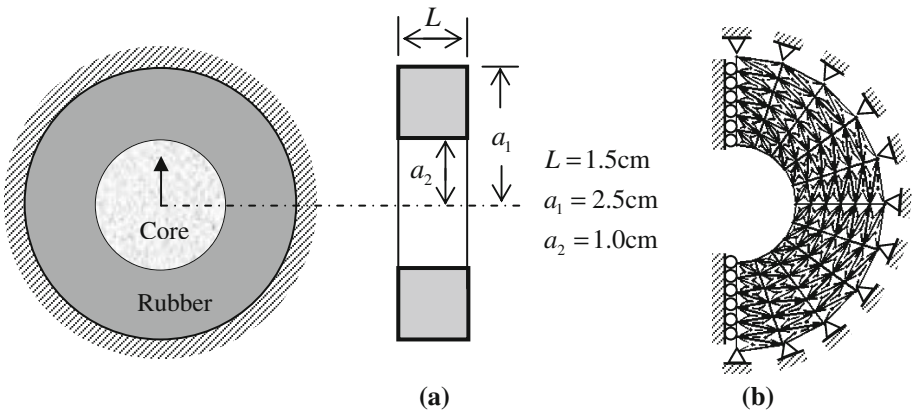

Fig. 21 Rubber bushing: **a** problem description; **b** half model discretized by HCTRM

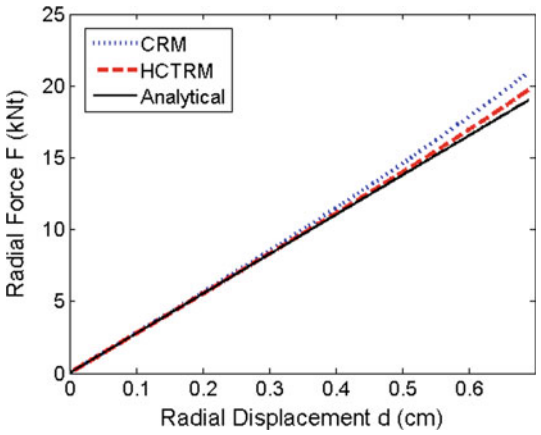

Fig. 22 Load–displacement curves of rubber bushing problem

obtained using Q1-SR as shown in Fig. 14a when uniform mesh is adopted. The checkerboard patterns are less pronounced but still visible in a non-uniform mesh of Q1-SR as displayed in Fig. 14b. In comparison with Q1-SR, CRM and HCTRM are entirely free from spurious checkerboarding. CRM and HCTRM generate similar pressure solution in both uniform and non-uniform meshes.

In Fig. 15, the pressure distributions at $y = 0.5$ obtained by Q1-SR does not even reproduce the sinusoidal-like pressure characteristic of the problem. In contrast, both CRM and HCTRM generate much better pressure distributions than Q1-SR, as shown in Fig. 15. Figure 16 shows two-level partition schemes pass the numerical inf-sup test in this problem whereas Q1-SR fails to satisfy the inf-sup test.

5.4 Cook's membrane problem

Cook's membrane model is a classical benchmark problem used to examine whether the numerical method is likely to provide a locking-free and non-oscillating solution in nearly incompressible material under combined shear and bending deformation. The geometry and boundary condition are shown in Fig. 17a. The left side boundary is fully constrained, and the right side boundary is subjected to a uniform distributed vertical traction. A typical discretization of CRM and HCTRM is plotted in Fig. 17b. Non-uniform meshes of CRM and HCTRM are also considered in this example. They are shown in Fig. 17c.

Figure 18 compares the variation of the vertical displacement of the upper right corner as mesh is refined. Both HCTRM and Q1-SR converge to the same solution as mesh is refined. On the other hand, CRM appears to be stiffer than HCTRM and Q1-SR. Although CRM performs well in the previous three examples, it does exhibit volumetric locking in this example.

Figure 19 show the pressure distribution using 8×8, 16×16 semi-uniform meshes, and non-uniform mesh. As we can see, Q1-SR and CRM results exhibit severe pressure oscillation. Among the three, HCTRM obtains the most desirable pressure field. Numerical inf-sup test, shown in Fig. 20, indicates that HCTRM is stable as mesh is refined. Although Q1-SR is free of locking, it does suffer from pressure oscillation as it fails to meet the inf-sup stability condition. On the other hand, the failure to pass inf-sup test in CRM reflects its inability to produce locking and oscillation-free solution in this example.

5.5 Radial bushing of rubber cylinder

In this example, the nonlinear performance of the proposed two-level partition schemes is evaluated. The hyper-elastic characteristic of rubber material is described by the Mooney–Rivlin strain energy density function with material constants [12] given by

$$\begin{aligned} A_{10} &= 0.2599\,\text{MPa} \\ A_{01} &= 0.1608\,\text{MPa} \end{aligned} \tag{60}$$

The bulk modulus is taken to be 1.0×10^5 MPa which is corresponding to the Poisson ratio $\upsilon = 0.4999958$ in the linear elasticity problem.

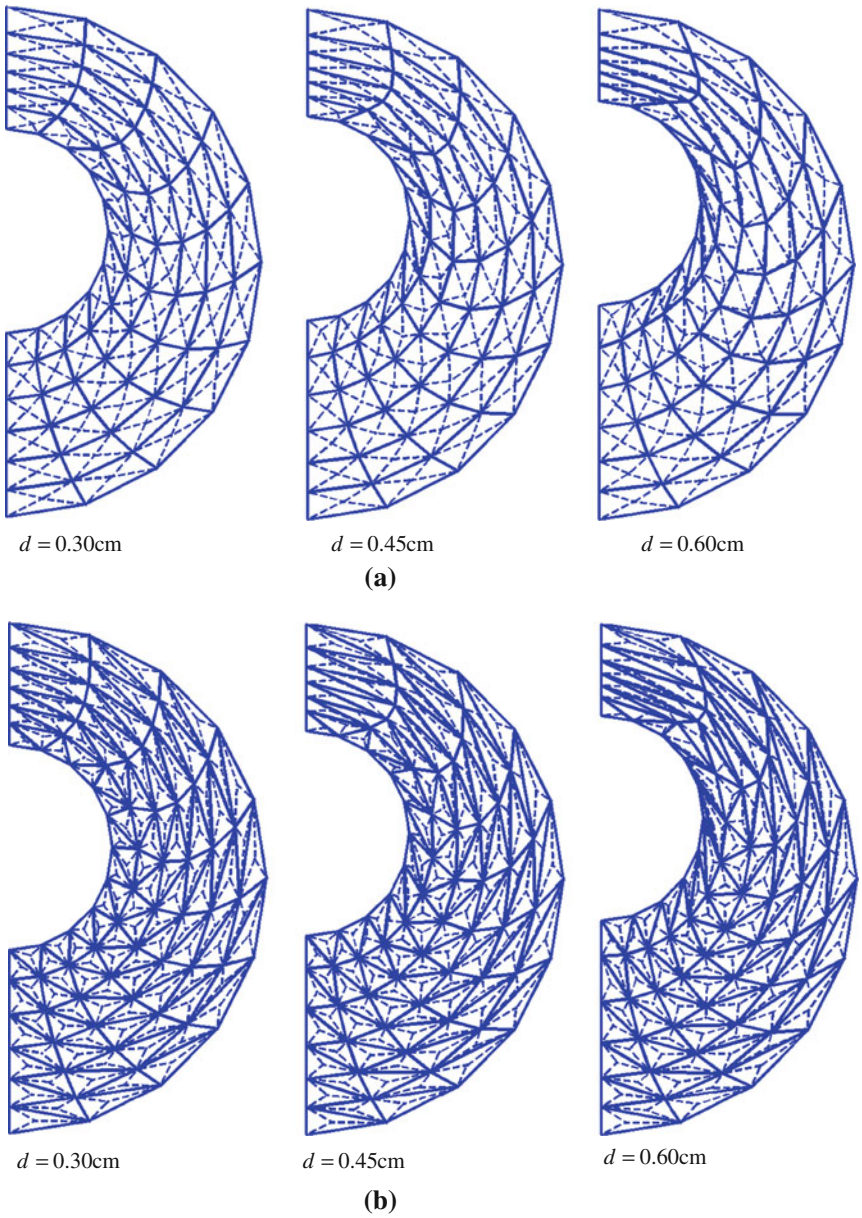

Fig. 23 Deformation of rubber insertion. **a** CRM. **b** HCTRM

The radial bushing problem, as shown in Fig. 21a, is analyzed, where the outer surface is fixed, and the inner surface of rubber cylinder sticks with an un-deformed core moving along vertical direction. Under the plane strain assumption, the linear relationship between radial force F and displacement d has been studied by Stevenson [37] as follows

$$F = \frac{8\pi\,(A_{10} + A_{01})\left(\beta^2 + 1\right) Ld}{\left(\beta^2 + 1\right)\ln\beta - \left(\beta^2 - 1\right)} \tag{61}$$

where $\beta = a_1/a_2$, $a_1 = 2.5\,\text{cm}$ and $a_2 = 1.0\,\text{cm}$ are the outer and inner radius of the un-deformed cylinder, and L is the shape factor, as shown in Fig. 21a. Considering the symmetry of the problem, we model half of the 2D cross-section. The discretization of HCTRM is plotted in Fig. 21b.

The load–displacement curves generated by two partition schemes are shown in Fig. 22. HCTRM result shows a linear load–displacement growth within the bushing operating range, which agrees well with analytical solution. Compared to HCTRM, CRM obtains slightly stiffer response in the nonlinear range. Nonlinear response in both results occurs as the top inner surface is pushed very close to the outer surface.

Figure 23 provides the deformation history of CRM and HCTRM. It is observed that both methods obtain smooth displacement field. The hydrostatic pressure contour plots

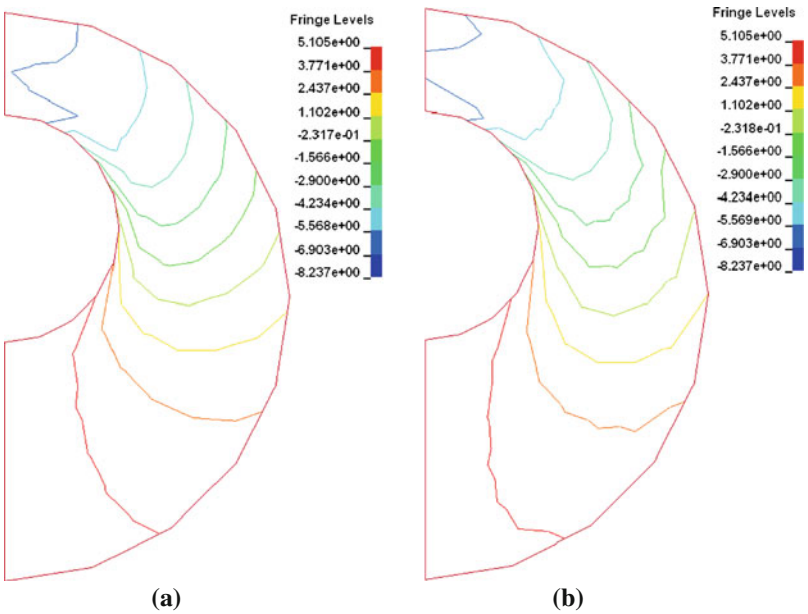

Fig. 24 Hydrostatic pressure contour for rubber bushing problem. **a** CRM. **b** HCTRM

shown in Fig. 24 confirm that CRM and HCTRM are simultaneously free of locking and checkerboarding in this nonlinear problem.

6 Conclusion

A novel approach for repartitioning existing lower-order finite element mesh for the linear and nonlinear volumetric locking-free analysis has been presented. Two types of finite element mesh originally discretized by quadrilateral and triangular elements are investigated in this study. The repartitioned mesh is composed of linear sub-triangular elements with non-overlapping strain/gradient smoothing performed on the pairs of adjacent elements. Several numerical examples have been studied to evaluate their applicability to the volumetric locking-free analysis. The stability of the resulting mixed finite element scheme has been examined through the numerical inf-sup test.

Our numerical results have shown that the repartitioned mesh based on triangular elements has successfully delivered volumetric locking-free solution and passed the numerical inf-sup test in all four linear benchmarks. The approach also appears to be quite robust in dealing with large deformation in the nonlinear analysis. In contrast, although the repartitioned mesh based on quadrilateral elements achieves comparable accuracy in most cases, it does exhibit volumetric locking and pressure oscillation in Cook's membrane problem. The volumetric locking and pressure oscillation solution of repartitioned mesh based on quadrilateral elements is consistent with its failure to pass the numerical inf-sup test in same example. This result suggests that the repartitioned mesh based on quadrilateral elements does not yield a uniform inf-sup condition and therefore the optimal performance is not guaranteed.

The main advantage of the proposed approach lies in its simplicity to be fitted into the conventional displacement-based finite element code and solved by the standard direct solver. Additionally, since the mesh repartitioning scheme does not involve a new discretization on the boundary, the boundary, contact and constraint conditions remain the same as in the original setting. Those unique features make the proposed approach as an attractive alternative to the finite element analysis of near-incompressible problems in the industrial applications. The mesh repartitioning scheme in three-dimensional case and its application to the nonlinear analysis of rubber compounds will be the subject of a forthcoming paper. The approach could also be a promising alternative for use in adaptive finite element method involving near-incompressible path-dependent materials. Application such as the r-adaptive finite element method using tetrahedral elements in the metal forging and extrusion simulations will be studied in the near future. The improvements of repartitioning scheme based on quadrilateral elements will also be considered in the future.

Acknowledgment The support of this research by LSTC and Yokohama Rubber Co., Ltd, Japan is gratefully acknowledged.

References

1. Andrade Pires FM, de Souza Neto EA, de la Cuesta Padilla JL (2004) An assessment of the average nodal volume formulation for the analysis of nearly incompressible solids under finite strains. Int J Numer Methods Eng 20:569–583

2. Areias P, Matouš K (2008) Stabilized four-node tetrahedron with nonlocal pressure for modeling hyperelastic materials. J Numer Methods Eng 76:1185–1201
3. Arnold DN, Brezzi F, Franca LP (1984) A stable finite element for the Stokes equations. Calcolo 21:337–344
4. Arnold DN, Brezzi F, Cockburn B, Marini LD (2001) Unified analysis of discontinuous Galerkin methods for elliptic problems. SIAM J Numer Anal 39:1749–1770
5. Auricchio F, Beiraode Veiga L, Buffam A, Lovadina C, Reali A, Sangalli G (2007) A fully locking-free isogeometric approach for plane linear elasticity problems: a stream function formulation. Comput Methods Appl Mech Eng 197:160–172
6. Bathe KJ (1996) Finite element procedures. Prentice-Hall, New Jersey
7. Babuška I (1973) The finite element method with Lagrangian multipliers. Numer Math 20:179–192
8. Belytschko T, Lu YY, Gu L (1994) Element-free Galerkin methods. Int J Numer Methods Eng 37:229–256
9. Belytschko T, Liu WK, Moran B (2001) Nonlinear finite elements for continua and structures, 3rd edn. Wiley, New York
10. Bonet J, Burton AJ (1998) A simple average nodal pressure tetrahedral element for incompressible and nearly incompressible dynamic explicit applications. Commun Numer Methods Eng 14:437–449
11. Brezzi F, Fortin M (1991) Mixed and hybrid finite element methods, Srpringer Series in Computational Mathematics Vol. 15. Springer, New York
12. Chen JS, Wu CT, Pan C (1996) A pressure projection method for nearly incompressible rubber hyperelasticity, Part II: applications. J Appl Mech 63:869–876
13. Chen JS, Yoon S, Wang HP, Liu WK (2000) An improved reproducing kernel particle method for nearly incompressible finite elasticity. Comput Methods Appl Mech Eng 181:117–145
14. Chen JS, Wu CT, Yoon S, You Y (2001) A stabilized conforming nodal integration for Galerkin mesh-free methods. Int J Numer Methods Eng 50:435–466
15. Crouzeiz M, Raviart PA (1973) Conforming and nonconforming finite element methods for solving the stationary Stokes equations. RAIRO Sér Rouge 7:33–75
16. De S, Bathe KJ (2001) Displacement/pressure mixed interpolation in the method of finite spheres. Int J Numer Methods Eng 51:275–292
17. Dolbow J, Belytschko T (1999) Volumetric locking in the element free Galerkin method. Int J Numer Methods Eng 46:925–942
18. Elguedj T, Bazilevs Y, Calo VM, Hughes TJR (2008) $\overline{B}$ and $\overline{F}$ projection methods for nearly incompressible linear and non-linear elasticity and plasticity using higher-order NURBS elements. Comput Methods Appl Mech Eng 197:2732–2762
19. Hansbo P, Larson M (2002) Discontinuous Galerkin methods for incompressible and nearly incompressible elasticity by Nitsche's method. Comput Methods Appl Mech Eng 191:1895–1908
20. Hauret P, Kuhl E, Ortiz M (2007) Diamond elements: a finite element/discrete-mechanics approximation scheme with guaranteed optimal convergence in incompressible elasticity. Int J Numer Methods Eng 72:253–294
21. Hughes TJR (2000) The finite element method. Prentice-Hall, Englewood Cliffs, NJ
22. Hughes TJR, Franca P, Balestra M (1986) A new finite element formulation for fluid dynamics, V. Circumventing the Babuška-Brezzi condition: a stable Petrov-Galerkin formulation of the Stokes problem accommodating equal order interpolation. Comput Methods Appl Mech Engrg 59:85–99
23. Hughes TJR, Cottrell JA, Bazilevs Y (2005) Isogeometric analysis: CAD, finite elements, NURBS, exact geometry and mesh refinement. Comput Methods Appl Mech Eng 194:4135–4195
24. Krysl P, Zhu B (2008) Locking-free continuum displacement finite elements with nodal integration. Int J Numer Methods Eng 76:1020–1043
25. Lamichhane BP (2009) Inf-sup stable finite element pairs based on dual meshes and bases for nearly incompressible elasticity. IMA J Numer Anal 29:404–420
26. Liu WK, Ong JSJ, Uras RA (1986) Finite element stabilization matrices—a unification approach. Comput Methods Appl Mech Eng 53:13–46
27. Liu WK, Jun S, Li S, Adee J, Belytschko T (1995) Reproducing kernel particle methods for structural dynamics. Int J Numer Methods Eng 38:1655–1679
28. Lovadina C, Auricchio F (2003) On the enhanced strain technique for elasticity problems. Comput Struct 81:777–787
29. Malkus DS, Hughes TJR (1978) Mixed finite element methods-reduced and selective integration techniques: a unification of concepts. Comput Methods Appl Mech Eng 15:63–81
30. Oden JT, Kikuchi N, Song YJ (1982) Penalty-finite element methods for the analysis of Stokesian flows. Comput Methods Appl Mech Eng 31:297–329
31. Ortiz A, Puso MA, Sukumar N (2010) Maximum-Entropy meshfree method for compressible and near-incompressible elasticity. Comput Methods Appl Mech Eng 199:1859–1871
32. Park CK, Wu CT, Kan CD (2011) On the analysis of dispersion property and stable time step in meshfree method using the generalized meshfree approximation. Finite Elem Anal Des 47:683–697
33. Puso MA, Solberg J (2006) A stabilized nodally integrated tetrahedral. Int J Numer Methods Eng 67:841–867
34. Simo JC, Hughes T (1986) On the variational foundation of assumed strain methods. ASME J Appl Mech 53:51–54
35. Simo JC, Rifai MS (1990) A class of mixed assumed strain methods and the method of incompatible modes. Int J Numer Methods Eng 29:1595–1638
36. Stenberg R (1990) Error analysis of some finite element methods for the Stokes problem. Math Comput 54:495–508
37. Stevenson AC (1943) Some boundary problems of two-dimensional elasticity. Philos Mag 34:766–793
38. Timoshenko SP, Goodier JN (1970) Theory of elasticity, 3rd edn. McGraw-Hill, New York
39. Vidal Y, Villon P, Huerta A (2003) Locking in the incompressible limit: pseudo-divergence-free element free Galerkin. Commun Numer Methods Eng 19:725–735
40. Washizu K (1982) Variational methods in elasticity and plasticity, 3rd edn. Pergamon Press, New York
41. Wriggers P, Mueller-Hoeppe DS, Loehnert S (2009) Brick elements for finite deformations based on macro-concepts and on inhomogeneous enhancement. Comput Methods Appl Sci 14: 33–48
42. Wu CT, Hu W (2011) Meshfree enriched simplex elements with strain smoothing for the finite element analysis of compressible and nearly incompressible solids. Comput Methods Appl Mech Eng 200:2991–3010
43. Wu CT, Koishi M (2009) A meshfree procedure for the microscopic analysis of particle-reinforced rubber compounds. Interact Multiscale Mech 2:147–169
44. Wu CT, Park CK, Chen JS (2011) A generalized meshfree approximation for the meshfree analysis of solids. Int J Numer Methods Eng 85:693–722
45. Zienkiewicz OC, Taylor RL (1987) The finite element method, 3rd edn. McGraw-Hill, London